Y. Guo, M. Lin, W. Lin, S. Zheng and M. L. N. Chen, "Microwave Photonic-Based Step Frequency Reflectometry for Electronic Circuit Defect Detection," in IEEE Transactions on Microwave Theory and Techniques, vol. 73, no. 8, pp. 5327-5339, Aug. 2025 is available at https://doi.org/10.1109/TMTT.2025.3542225.

Microwave Photonics-based Step Frequency Reflectometry for Electronic Circuit Defect Detection

Yiling Guo, Mingtuan Lin, Wei Lin, *Senior Member, IEEE*, Shilie Zheng, *Member, IEEE*, and Menglin L.N. Chen, *Senior Member, IEEE*

Abstract

In this study, a microwave photonic-based wideband step frequency (SF) reflectometry (MPSR) system, with centimeter range resolution, is presented to identify the interconnect defects in electronic circuits. Interconnect defects encompass a range of issues, including faulty solder joints, damaged cables, and insufficient bonding, all of which can manifest as impedance mismatches within the circuit. The defect detection procedure consists of two main steps: wideband step frequency signal generation based on optical frequency shift loop (OFSL) technique and the frequency response measurement of device under test (DUT). The wideband SF signal generated from OFSL can be employed as stimulus for frequency sweep measurement, facilitating the characterization of DUT by extracting its frequency response. Subsequent application of the inverse fast fourier transform (IFFT) to the measured frequency response enables the derivation of time-domain information, which is inherently linked to the location of discontinuities within DUT. The mathematical expression for frequency response is developed, and simulations of electronic and photonic systems are used to analyze the performance of the proposed concept. Following this, a proof-of-concept experiment was conducted to validate the theoretical framework, demonstrating the practical viability. An SF signal with bandwidth of 16 GHz is obtained, ensuring a high range resolution of approximately 6.3 mm. The discontinuities of four fabricated circuits are further accurately identified, showing a high degree of concordance with the results from vector network analysis (VNA). Compared to existing methods, the proposed system presents a cost-effective solution for detecting defects in electronic circuits, offering a non-destructive and rapid technique for identifying and diagnosing faults.

Index Terms

Microwave photonic, optical frequency shift loop (OFSL), reflectometry, step frequency (SF) signal, defect detection.

I. INTRODUCTION

Benefiting from the rapid progress in semiconductor and integrated circuit technology, the electronic device has shrunk to tiny size and compact structure, making the connections between electronics more complicated and delicate. Consequently, efficient and effective defect detection and location methods are crucial to ensure the reliability, safety, and performance of electronic devices.

Much effort has been put in this field and many researchers have demonstrated various methods in circuit defects detection. X-ray microscopy (XRM) is widely used in detecting internal defects due to its superior penetration ability, allowing for the capture of high resolution images to reveal internal structure [1], [2]. However, this method has its limitations when evaluating circuit connection performance, as the static imaging nature restricts its ability to capture the dynamic behavior of electrical signal. Moreover, high-energy exposure may destroy sensitive components in electronics. Another powerful detection technique, near-field measurement is widely used in radiation measurement [3]. Near-field measurement offers a means of acquiring field distribution data, which can be used through inversion algorithm to reconstruct the intensity and position of radiation sources. By leveraging the source reconstruction method and the difference method (DM-SRM), the source distribution can be accurately reconstructed, allowing for

Y. Guo, M. Chen and W. Lin are with Department of Electrical and Electronic Engineering, Hong Kong Polytechnic University. M. Lin is with College of Electronic Science and Engineering, National University of Defense Technology. S. Zheng is with the College of Information Science and Electronic Engineering, Zhejiang University. (Corresponding author: Menglin Chen, menglin.chen@polyu.edu.hk; Mingtuan Lin, linmingtuan08@163.com)

effective defect localization and identification [4]. In recent years, deep-learning techniques have gained widespread adoption in microwave circuit modeling and designing, as demonstrated in [5], [6], with applications also extending to the detection of defects within circuits. Specifically, deep learning-based automated optical inspection (AOI) is another method to achieve fault detection on electronic circuit, which utilize training datasets to effectively identify and diagnose faults, including missing or faulty components and solder joint defects [7]–[10]. However, in order to generate accurate model, substantial training data and significant computational resources are required and the accuracy of the model are subjected to image quality and circuit surface cleanliness. Moreover, the defect analysis is restricted to static image and does not consider the electrical behavior of circuit, neglecting the impact of defects on the circuit's functional performance.

Employing the microwave as detection source, reflectometry is a common nondestructive technique to capture the electrical characteristics of the circuit, which has been extensively investigated and applied in many electrical systems. Reflectometry techniques are categorized based on the analysis domain of the reflectometry response. By applying a short rise-time pulse or step voltage signal to the DUT and measuring its electrical response, time-domain reflectometry (TDR) [11] is a common method in defect detection. Evolved from traditional TDR, sequence time-domain reflectometry (STDR) and spread spectrum time-domain reflectometry (SSTDR) leverage a sequence of pulses to enhance the measurement resolution and accuracy, enabling more precise fault location [12]–[14]. While TDR measurements offer numerous advantages, the generation of short rise-time pulses presents a notable technical hurdle, particularly in high-frequency applications, where high degree of precision and accuracy in the pulse rise-time are paramount. Alternatively, frequency domain reflectometry (FDR) [15], [16] is another easily available technique to achieve defect detection by transforming the measured frequency response into time domain. Step frequency waveform reflectometry (SFWR) [17], [18] , using arbitrary waveform generator for signal generation, were designed for defect detection of long cables in power systems, with MHz level bandwidth (about 60 MHz) and meter level resolution. The SFWR systems show excellent measurement performance in long cable defect detection, however, it can not be used in the integrated electronic circuit. A high resolution usually requires specialized VNA with bandwidth more than 20 GHz, increasing the cost of detection and limiting its widespread use.

Benefiting from the ultra-wide bandwidth at optical frequencies (typically at hundreds of terahertz), the microwave photonics technique has emerged as a promising method for wideband signal generation [19]–[22] and processing [23]–[25], which opens up new avenues in radar system for ranging and imaging [26]–[31], as well as in medical applications [32]. In [33], an ultra-broadband SF signal generation based on optical frequency shift loop (OFSL) technique has been proposed, demonstrating superior wideband signal generation for radar applications [34]–[37]. Specifically, SF signal is generated through recirculating an input optical pulse signal in a frequency-shifting loop, in which the input signal is shift simultaneously by time and frequency with fixed increment in each circulation. The photonic-based wideband SF signal generation technology inspires the idea of photonic-based high-resolution reflectometry. As mentioned above, photonics-based SF radar has demonstrated superior performance in ranging and imaging. We innovatively adapt this photonic-based wideband signal generation mechanism to reflectometry technique, allowing for the detection of circuit defects. The wideband SF signal can be used as a reference signal in reflectometry technique to characterize the electrical properties of the DUT in a non-invasive and non-destructive manner, which enables the detection of defects and faults within the DUT.

The structure of this article is organized as follows. In Section II, the proposed MWP-based SF signal reflectometry system is introduced. Section III and IV provide a detailed theoretical analysis of the proposed system, focusing on the principles of wideband signal generation and frequency response measurements, which form the foundation of the system configuration. Moreover, simulations of electronic and photonic system are also employed to assess the feasibility of the proposed system. The experiment setup and result analysis are discussed in Section V, followed by the conclusion in Section VI.

II. STRUCTURE AND PRINCIPLE OF MWP-BASED STEP FREQUENCY REFLECTOMETRY

Fig. 1 illustrates the system structure of the MPSR fault detection technique, which contains two units. The first unit is wideband SF signal generation, which consists of three key components: (1) a high-speed optical switch, comprising an RF signal-driven acousto-optic modulator (AOM); (2) optical SF signal generation via OFSL; (3) time-domain heterodyne beating to generate microwave SF signal in photodetector. The second unit

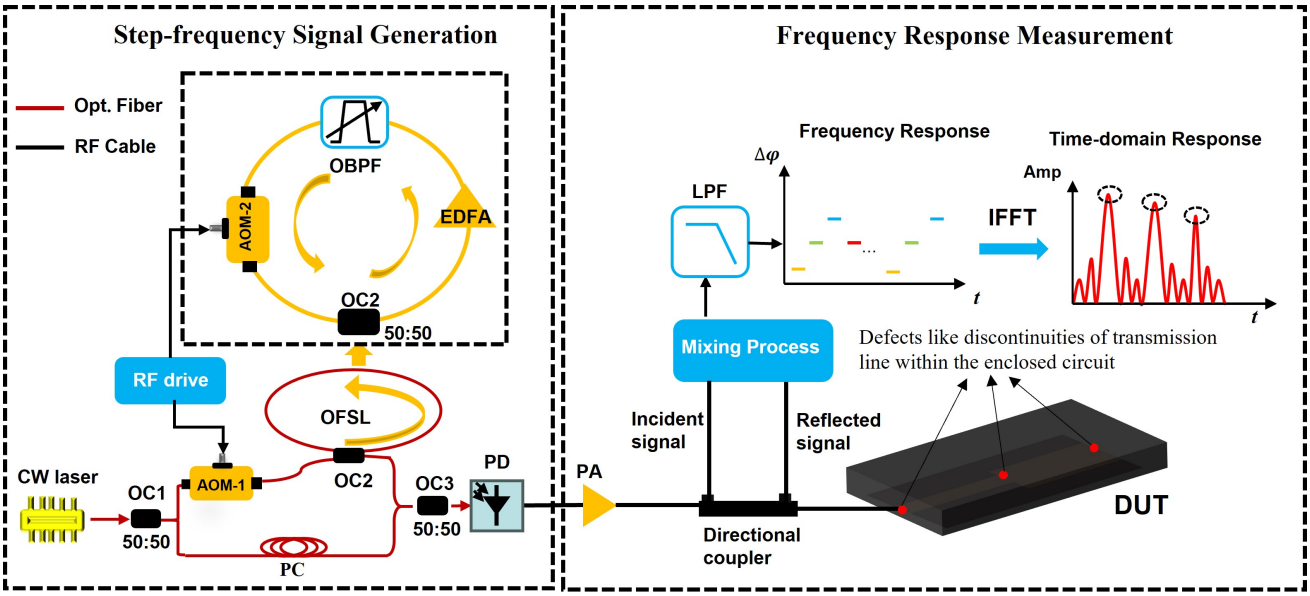

Fig. 1. System configuration of the MPSR detection technique. OFSL, optical frequency shifting Loop; RF, radio-frequency; OBPF, optical bandpass filter; LPF, lowpass-filter; EDFA, erbium-doped fiber amplifier; AOM, acousto-optic modulator; OC, optical coupler; PD, photodetector.

is frequency response measurement to extract the phase delay information encoded in the reflected signal of DUT. In principle, the frequency response of a DUT can be derived by mixing the incident and the reflected signals, and subsequently converting the result into time domain via IFFT, which enables the spatial identification and localization of discontinuities within the DUT. Specifically, the generation of SF signal is accomplished through recirculating an optical pulse signal within an OFSL. The pre-generated-SF signal is subsequently utilized as incident signal and propagate through the DUT. The frequency response measurement of the DUT is performed through heterodyne mixing process, wherein the incident and reflected signal are coherently mixed to extract the electronic characteristic. A demodulated signal, encoding the phase difference between the echo signal and the incident signal, is obtained after the mixing process, which is then followed by a lowpass-filter (LPF) to remove harmonic high frequency spurs. The frequency of the response signal is pretty low and can be easily acquired and processed. Eventually, the application of IFFT transformation to the response signal allows for the extraction of time delay information, which is inherently linked to the location of discontinuities within the DUT. The IFFT spectrum provides a temporal map of the DUT's frequency response, as illustrated in Fig. 1, with peaks corresponding to the individual discontinuity within the DUT, demonstrating the feasibility of the proposed system in the determination of the discontinuities. A more in-depth examination of the system configuration is provided in Sections III and IV.

III. WIDEBAND STEP FREQUENCY SIGNAL GENERATION

In reflectometry applications, a wider probe signal bandwidth directly correlates with higher resolution, making broad bandwidth signals highly desirable. The SF signal described here is generated through a recirculating OFSL, as diagrammed in Fig. 1. The continuous wave (CW) laser signal is converted into an initial rectangular optical pulse signal via an AOM (AOM-1). This AOM is driven by MHz-level RF signal and the temporal duration time of the driving signal at AOM-1 is precisely adjusted to coincide with the propagation time in each circulation to reduce the interference of adjacent pulse. The second AOM (AOM-2) is employed to incrementally shift the center frequency of the optical pulse, introducing a frequency increment of Δf. An erbium-doped fiber amplifier (EDFA) is employed to compensate for the coupling losses. An optical bandpass filter is used to control the spectral range of the output signal and suppress unwanted noise. Consequently, the output of the OFSL at is a series of discrete sub-pulses. This sub-pulse signal is then down-converted to the RF domain through time-domain heterodyne beating process via photodetector.

In summary, the input signal of OFSL undergoes a dual transformation at each circulation, where it is simultaneously shifted in time by τ and in frequency by Δf. After N iterations, the output signal of the OFSL is

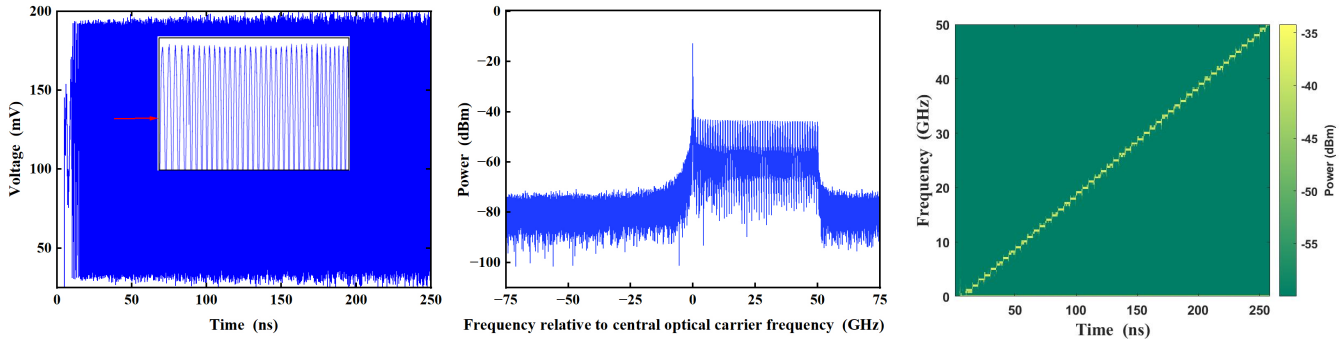

(a) (b) (c)

Fig. 2. Simulated wideband SF signal. (a) Temporal waveform of the OFSL output signal, (b) frequency spectrum of the OFSL output, and (c) time frequency spectrum from STFT.

composed of the seed optical signal and the sum of N time frequency-shifted replicas of the rectangular pulse. The resulting signal is subsequently processed via heterodyne beating using a photodetector, generating SF signal in the microwave domain with the total bandwidth of $N\Delta f$. This SF signal exhibits a linear frequency sweep, with a bandwidth that is directly proportional to the number of circulations, demonstrating the capability of wideband signal generation with well-defined spectral profile.

To evaluate the feasibility of the proposed system, we conduct simulations using photonic and microwave circuit co-simulator. Leveraging advancements in photonics and electronic software, these simulations provide a more in-depth understanding of the complex interactions between electronic and photonic components, which allows us to pinpoint potential problems, refine our design, and lay the groundwork for experimental setup.

The first simulation is designed to illustrate the system's capacity to generate SF signal, serving as a foundation for further analysis. The simulation parameters were set as follows: frequency deviation of AOM Δf = 1 GHz; round trip delay of the OFSL τ= 5 ns (remaining constant for all simulations); gain of ideal EDFA G=3 dB; number of circulations N = 50. Fig. 2 presents the simulation results. The temporal waveform of OFSL output signal is depicted in Fig. 2(a), spanning a time duration of approximately 250 ns. Fig. 2(b) displays the spectrogram of the measured microwave signal, which spans a frequency range of 0-50 GHz, and exhibits a signal-to-noise ratio (SNR) of 30 dB. In addition, the spectrogram of the microwave SF signal is computed by short-term fourier transform (STFT), providing a time-frequency relationship of the generated SF signal that reveal its frequency content and temporal variation, as presented in Fig. 2(c). The generated signal exhibits a stepping pattern, starting at 1 GHz, hoping 1 GHz after every 5 ns and resetting for every 250 ns. The simulation results demonstrate the feasibility of the proposed system in synthesizing wideband SF signal. Moreover, the bandwidth of microwave SF signal can be flexibly modulated by adjusting bandwidth of OBPF in the OFSL.

IV. FREQUENCY RESPONSE MEASUREMENT AND DETECTION PRINCIPAL

The wideband SF signal generated beforehand can serve as the incident signal, propagating through the DUT to extract its electrical characteristic. The incident signal echoes back whenever it encounters the impedance discontinuous points, which usually occur as a result of faults, joints, and terminals. The magnitude and phase information of the reflected signals can be defined as the frequency response of the DUT. We define the optical signal injected in the OFSL as $E_{in} = E_0\exp(j2\pi f_c t)$, the output optical signal of OFSL after *k*-th circulation is

$$S_t = E_k\exp[j2\pi(f_c + k\Delta f)t + \theta_k] \tag{1}$$

where E_k and θ_k is the amplitude and phase of the *k*-th OFSL optical output signal, f_c is the frequency of the optical carrier signal, Δf is the incremental frequency. The SF signal in microwave domain is generated by the heterodyne beating via photodetector, given by

$$S_{sf}(t,k) = A_k\exp(j2\pi k\Delta f t + \theta_k) \tag{2}$$

where A_k and θ_k is the amplitude and phase of the *k*-th SF signal.

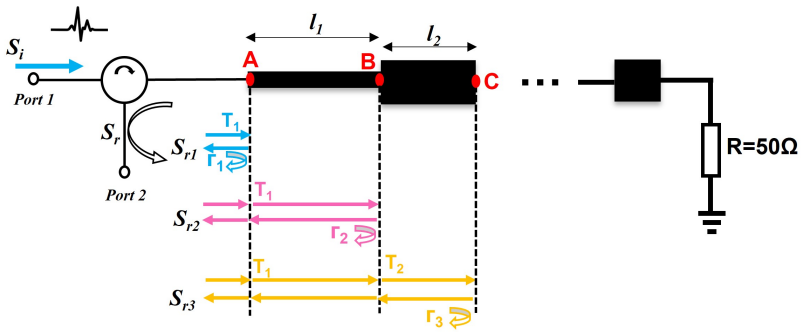

Fig. 3. Schematic diagram illustrating multiple reflections caused by multiple impedance mismatches.

Initially, we examine a scenario where a single impedance discontinuity is present within the DUT. Hence, the reflected signal of the DUT is given by

$$S_{sf}(t-\tau_d,k) = \Gamma A_k \exp[j2\pi k\Delta f(t-\tau_d)+\theta_k] \tag{3}$$

where Γ represents the reflection coefficient at the discontinuity, and τ_d denotes the time delay introduced by the discontinuity within DUT. This reflected signal is subsequently mixed with the input signal, as described by Equation (2), resulting in the frequency response of the DUT, expressed as

$$S_k = \Gamma \exp(-j2\pi k\Delta f\tau_d) \tag{4}$$

Equation (4) indicates that the frequency response of k-th sub pulse obtains a phase shift of $\Delta\phi = k\Delta f\tau_d$, which is stemmed from the time delay between the reference point and location of discontinuity. This linear relationship between frequency and phase shift sets up the foundation for extracting the location information of DUT. Once the time delay is provided, the distance can be recalculated with $\tau_d = \frac{2d}{v}$, where d is the distance between the reference point and discontinuity, and v is the travelling velocity of signal through specific transmission medium.

The frequency response of the DUT is the combination of response at each frequency, which is given by

$$FR = \{\Gamma_1 exp(-j2\pi\Delta f\tau_d), ...\Gamma_k \exp(-j2\pi k\Delta f\tau_d)...\} \tag{5}$$

For multiple discontinuities, it would occur multiple reflections. For the purpose of simplifying the analysis, a single reflection is assumed to occur at each discontinuity, denoted as S_{r1}, S_{r2}, S_{r3}, as shown in Fig. 3. However, it is worth noting that the same derivation can be extended to account for multiple reflections. The generated SF signal, as given by Equation (2), acts as the incident signal, which propagates through the DUT and it is reflected back upon encountering discontinuities. The transmission path of the signal within DUT, as illustrated in Fig. 3, can be described as follows: when the signal encounters the first discontinuity, it will be split into two parts: one that is partially reflected back with a reflection coefficient of Γ_1, and another that is partially transmitted with a transmission coefficient of T_1. The transmitted signal then travels a distance of l_1 before reaching the second discontinuity, where it is again partially reflected and partially transmitted. The reflected signal from the second discontinuity will then propagate back through the discontinuity at connection A, with a transmission coefficient of T_1. Consequently, the reflected signal at port 2, due to the reflection from the second discontinuity, can be represented as

$$S_{r2} = T_1^2\Gamma_2 A_k \exp(j2\pi k\Delta f(t-\frac{2l_1}{v})+\theta_k) \tag{6}$$

As previously shown, the transmitted signal at connection B will continue to propagate a distance of l_2, reaching the 3-rd discontinuity (connection C), where it will undergo another partial reflection and partial transmission. As a result, the reflected signal at port 2, due to the reflection from the third discontinuity, can be expressed as

$$S_{r3} = T_1^2T_2^2\Gamma_3 A_k \exp(j2\pi k\Delta f(t-\frac{2(l_1+l_2)}{v})+\theta_k) \tag{7}$$

where Γ_3 is the reflection coefficient of the third discontinuity, and T_2 is the transmission coefficient of the second discontinuity.

Similarly, the reflected signal at port 2, due to the reflection from the *n*-th discontinuity is given by

$$S_{rn} = \prod_{j=1}^{n-1} T_j^2 \Gamma_n A_k \exp(j2\pi k\Delta f(t - \frac{2\sum_{j=1}^{n-1} l_j}{v}) + \theta_k) \tag{8}$$

where Γ_n is the reflection coefficient of the *n*-th discontinuity, and T_j is the transmission coefficient of the *j*-th discontinuity.

Consequently, the total reflected signal of the *k*-th sub pulse at the reference point can be expressed as

$$\begin{aligned} S_r &= \Gamma_1 A_k \exp(j2\pi k\Delta f t + \theta_k) \\ &+ \sum_{n=2}^{N} \prod_{j=1}^{n-1} T_j^2 \Gamma_n A_k \exp(j2\pi k\Delta f(t - \frac{2\sum_{j=1}^{n-1} l_j}{v}) + \theta_k) \end{aligned} \tag{9}$$

Therefore, by launching a series of SF signal into the DUT and obtaining all the reflected signals over the given frequency sweeping, the frequency response of the *k*-th sub-pulse within the DUT, which contains N discontinuities, can be determined, as expressed by

$$S_k = \Gamma_1 + \sum_{n=2}^{N} \prod_{j=1}^{n-1} T_j^2 \Gamma_n \exp(-j2\pi k\Delta f \frac{2\sum_{j=1}^{n-1} l_j}{v}) \tag{10}$$

As a result of the above analysis, the frequency response measurement of the DUT can be extracted through heterodyne mixing process, where the incident and reflected signal are coherently mixed, yielding a demodulated signal that encodes the phase difference between the echo signal and the incident signal. The resulting frequency response is then transformed into the time domain using an IFFT transform, enabling the spatial identification and localization of discontinuities within the DUT.

A. Discontinuity Detection

In order to verify the feasibility of the proposed system, we utilize the generated broadband microwave SF signals into the application of discontinuity location. The simulation parameters are as follows: (1) permittivity of the substrate ε_r=9.6, (2) dielectric loss tangent of 0.001. The wide-band SF signal was first created using an optical simulator and subsequently injected into microwave circuit simulator to conduct co-simulation of optical system and electronic circuits. The schematic diagram for impedance discontinuities in common circumstances (open and short) and simulation results are shown in Fig. 4 . The wideband SF signal was injected into point A, and the incident signal S_i was transmitted along the microstrip line to the test terminal (point B), where it was rflected back as signal S_f due to the impedance mismatch at the terminal. In this simulation, the open-circuit and short-circuit faults were set 10 mm away from the injected point. By applying inverse Fourier transform, the frequency domain data is converted to the time domain, yielding the time reflection response of the DUT, as depicted in Fig.4(a) and (b). As it can be seen, the first peak occurs at the beginning of the microstrip line (point A), and the second peak is the response of the DUT at the end of microstrip line (point B). The IFFT time-series result accurately located the discontinuities, as expected, confirming the effectiveness of the proposed system in accurately detecting open-circuit and short-circuit faults. Moreover, to assess the accuracy of the proposed system, we compare the simulation results with the S-parameter measured by ADS simulation and transfer to time domain, which served as a benchmark for evaluating performance of the proposed system. The consistent response in Fig. 4 (blue line) further validates the accuracy and reliability of the proposed system in detecting open-circuit and short-circuit faults.

Subsequently, we explore the detection performance of the MPSR system in a wide range impedance mismatch circumstances: impedance increase, impedance decrease, cascaded impedance. The insets of Fig. 5 illustrate the schematic configuration employed in the simulation setup, in which 3 DUTs with varying microstrip lines of disparate widths are implemented to conduct a parametric study. Microstrip line of varying widths are utilized to emulate the discontinuities, while adjusting the length of the line to simulate the spatial separation between the

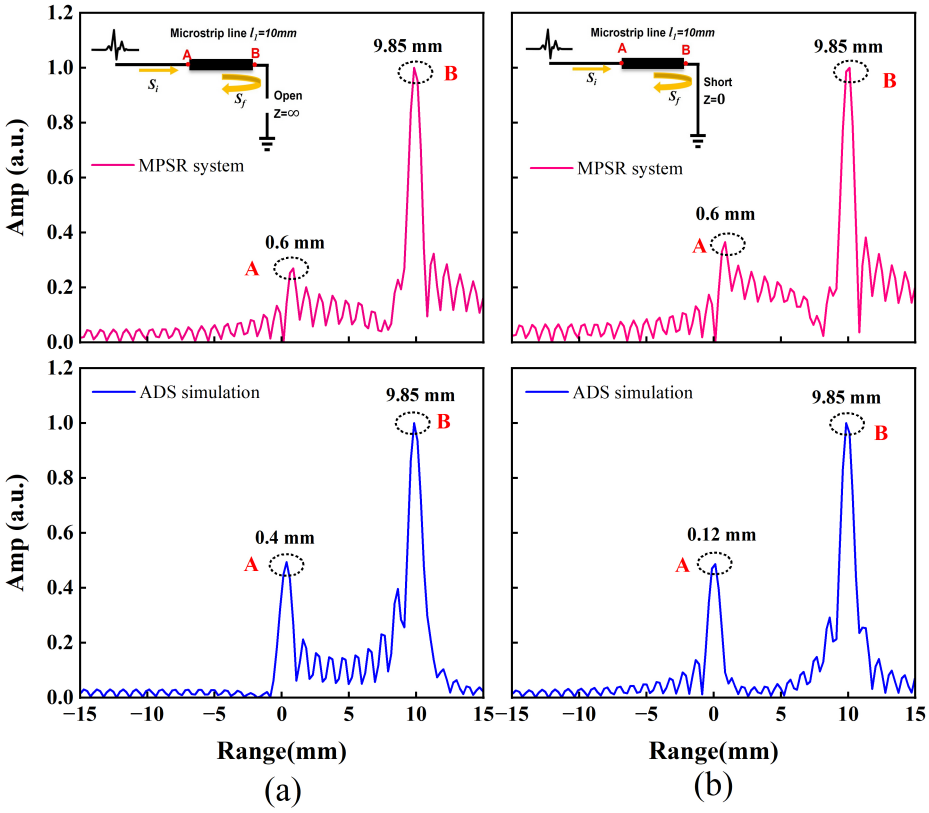

Fig. 4. IFFT results of MPSR system and ADS simulation. (a) Open-circuit and (b) Short-circuit.

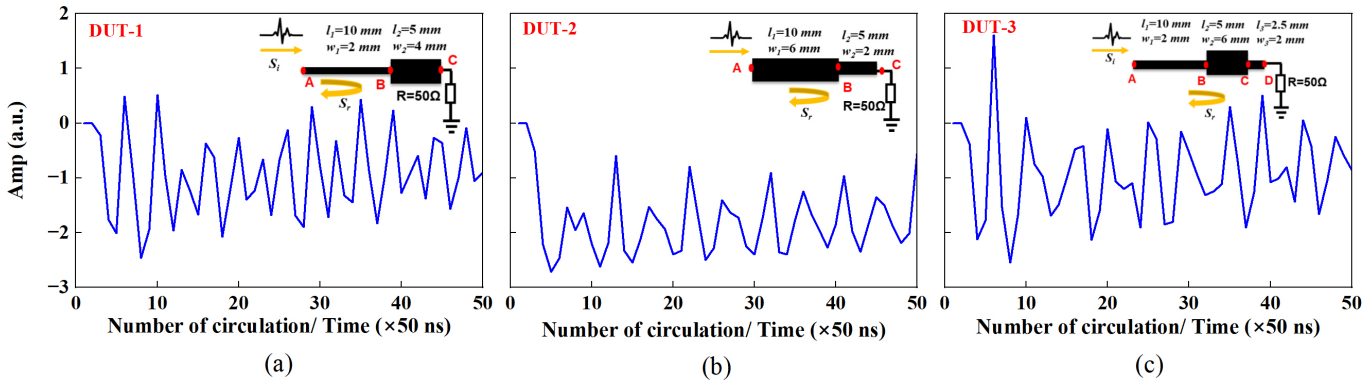

Fig. 5. Frequency response characteristics of (a) DUT-1, (b) DUT-2 and (c) DUT-3.

discontinuities. Specifically, DUT-1 is arranged in a pattern that decreases impedance, starting with a narrow line followed by a wider line, resulting in three discontinuities. DUT-2 is configured to exhibit an increasing impedance pattern, featuring a wide line initially, followed by a narrower line, which also introduces three discontinuities. DUT-3 is designed in pattern that decreases impedance first and then increases impedance, starting with a narrow line and transitioning to a wider line, and finally followed by a narrower line, creating four discontinuities. The wide-band SF signal was injected into the DUTs to obtain the frequency response, as presented in Fig. 5 (a)-(c). For DUT-1 simulation, the width of microstrip lines was 2 mm and 4 mm with the corresponding length of 10 mm and 5 mm, respectively. The pink line in Fig. 6(a) represents the result of the IFFT conversion of the frequency response obtained from the simulation of DUT-1. As it can be seen, the first peak occurs at the beginning of the microstrip line (connection A), and the second peaks is the response of the DUT at the second discontinuity (connection B), the third peak occurs at connection C. For DUT-2 simulation, the width of microstrip lines was 6 mm and 2 mm with the corresponding length of 10 mm and 5 mm. As expected, the IFFT results shown in Fig.

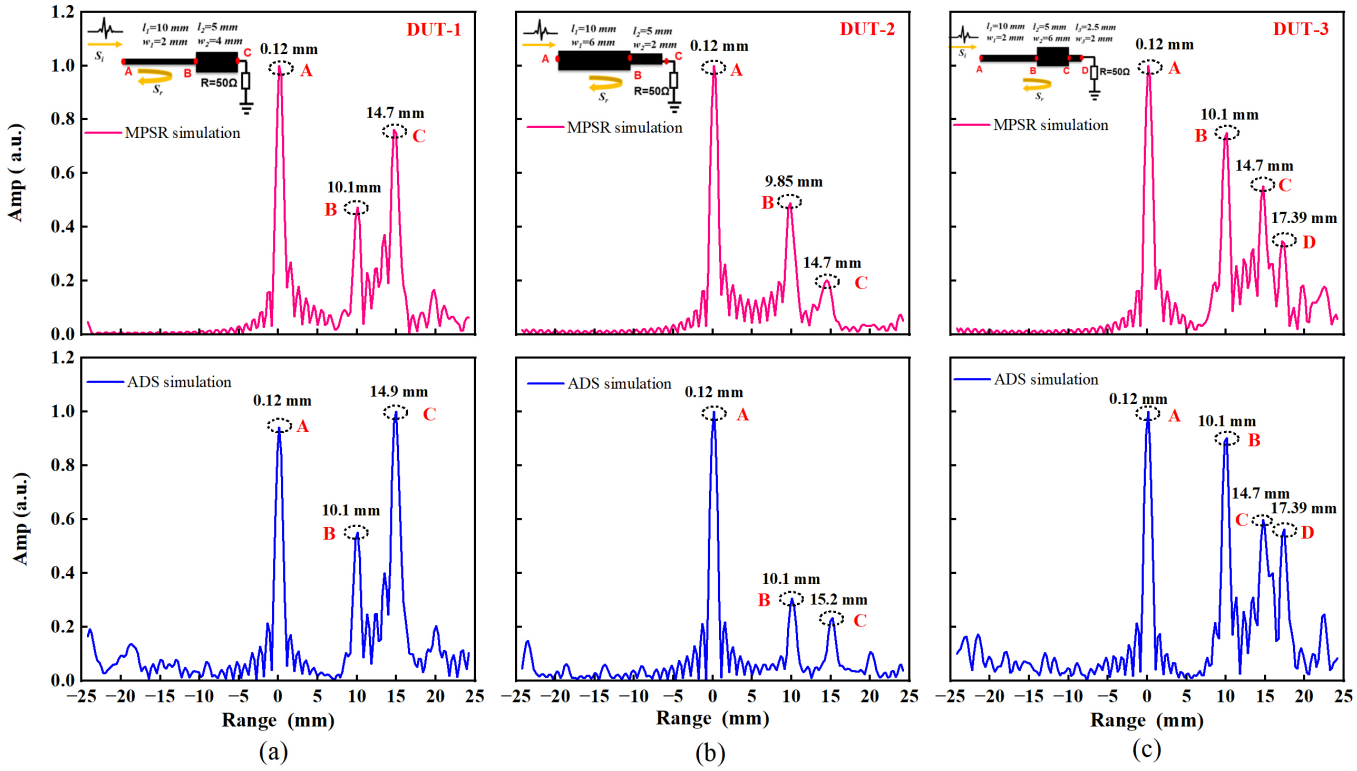

Fig. 6. IFFT results of MPSR system and ADS simulation. (a) DUT-1, (b) DUT-2 and (c) DUT-3.

6(b) (pink line) exhibit three distinct discontinuities, where the spacing between peaks corresponds to the spacing between discontinuities. For DUT-3 simulation, the width of microstrip lines was 2 mm, 6 mm and 2 mm, with the corresponding length of 10 mm, 5 mm and 2.5 mm. The IFFT results depicted in Fig. 6(c) (pink line) accurately identify the expected four discontinuities, with the the spacing between peaks corresponds to the spacing between discontinuities. In sum, the IFFT time-series result of three simulations accurately located the discontinuities, as expected, confirming the effectiveness of the proposed system. Moreover, to evaluate the accuracy of the proposed system, we conducted a comparative analysis between the S-parameter obtained from advanced design system (ADS) simulations, which were subsequently transformed into the time domain, and the results from the proposed system, using the ADS simulation as a benchmark for performance assessment. The proposed system's response exhibits excellent agreement with ADS simulation results, as depicted in Fig. 6(a)-(c) (blue line), with a maximum deviation of only 0.5 mm across all three scenarios, thereby validating the accuracy and reliability of the proposed system in detecting impedance mismatches.

B. Range Resolution and Detection Precision Analysis

To investigate the range resolution of the proposed system, a parametric study was conducted. The insets of Fig. 7 illustrate the schematic configuration employed in the simulation setup, which comprises 2 DUTs (DUT-1, DUT-4). DUT-1 serves as a reference unit, used for comparative analysis with other DUTs. Both DUTs were arranged in a pattern that decreases impedance, starting with a narrow line followed by a wider line, resulting in three discontinuities. For DUT-4, the microstrip lines also had widths of 2 mm and 10 mm, but with corresponding lengths of 10 mm and 1.5 mm, respectively. Consequently, the spatial separation between connection B and C reduced to 1.5 mm, allowing for a further assessment of the system' s range resolution capabilities. Fig. 7(a) and (b) compares the time domain response of the reflected signal from the above two DUTs, with incident SF signal featuring a bandwidth of 25 GHz. Notice that, in the case when the spatial distance between discontinuities is 1.5 mm, it becomes challenging to resolve the two discontinuities due to the limited range resolution. In order to obtain finer range resolution, one can increase the bandwidth of incident signal, as there is an inverse relationship between range resolution and bandwidth. Fig. 7(c) shows the ranging results obtained from the proposed system

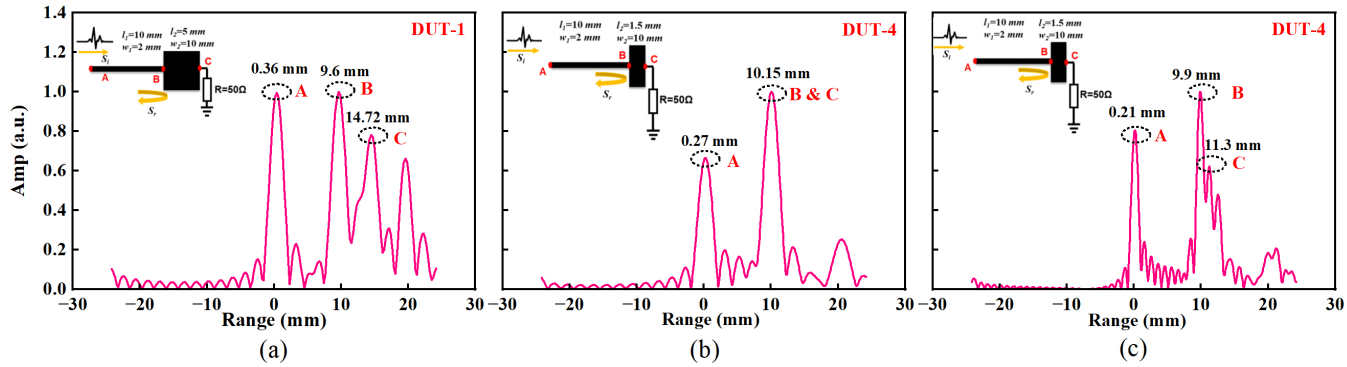

Fig. 7. Range resolution analysis of MPSR system with distance between discontinuities of (a) 10 mm and 5 mm (with 25 GHz bandwidth), (b) 10 mm and 1.5 mm (with 25 GHz bandwidth) and (c) 10 mm and 1.5 mm (with 50 GHz bandwidth).

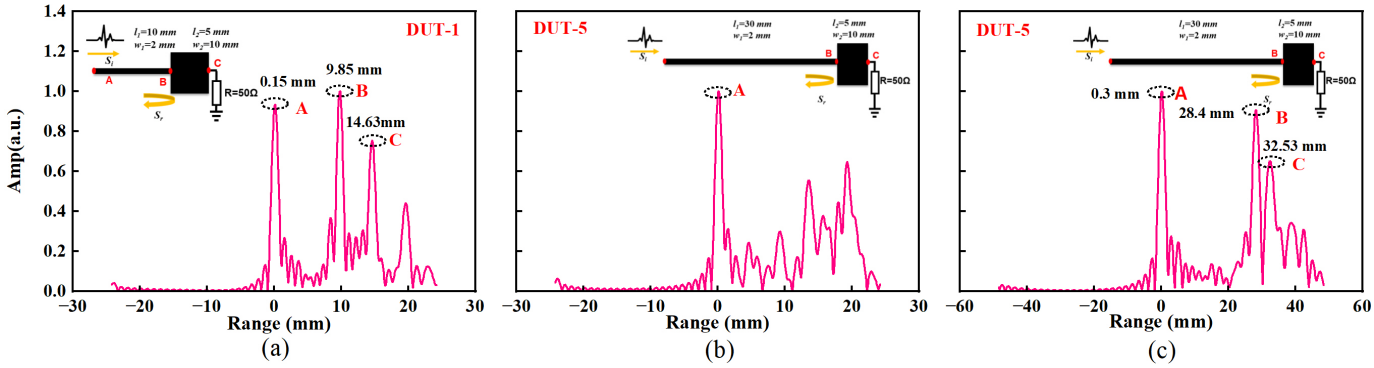

Fig. 8. Maximum unambiguous range analysis of MPSR system with distance between discontinuities of (a) 10 mm and 5 mm (with Δf= 1 GHz), (b) 30 mm and 5 mm (with Δf= 1 GHz) and (c) 30 mm and 5 mm (with Δf= 0.5 GHz).

with a bandwidth of 50 GHz. The precise location of discontinuities at connection B and C is accurately resolved, demonstrating a significant improvement in range resolution capacity as the bandwidth increases.

C. Maximum Unambiguous Range Analysis

As previous illustrated, the frequency response of DUT is a composite representation of all the reflected signal over the frequency range, which is analogous to frequency sampling. Frequency sampling can introduce the phenomenon of time aliasing, which arise from under sampling in frequency domain. When the frequency domain data is sampled, i.e., the frequency response is measured at discreate frequency points rather than continuously, the resulting time domain representation will repeat with a period of $1/\Delta f$,where Δf represents the frequency sampling interval. The duration of this repetition period denoted as the Nyquist period, defines the maximum unambiguous range (MUR) of the measurement that can be made without encounter time aliasing, as described in [38]. Therefore, to extend the measurement range, one can either increase the number of sampling points or reduce the frequency span. Both of these modifications will result in decrease of Δf, thereby increasing the time domain range. Notably, in a reflection measurement, the MUR is halved to $1/2\Delta f$, resulting from the round-trip propagation time between the discontinuity and the test port. In reflection measurement, the MUR calculation is given by

$$R = \frac{v}{2\Delta f} \tag{11}$$

where v is the traveling velocity of signal.

For a measurement with Δf =1 GHz, the corresponding time domain response exhibits a periodic repetition with a period of $1/2\Delta f$=0.5 ns , which implies time domain response will repeat every 0.5 ns. Using the microstrip

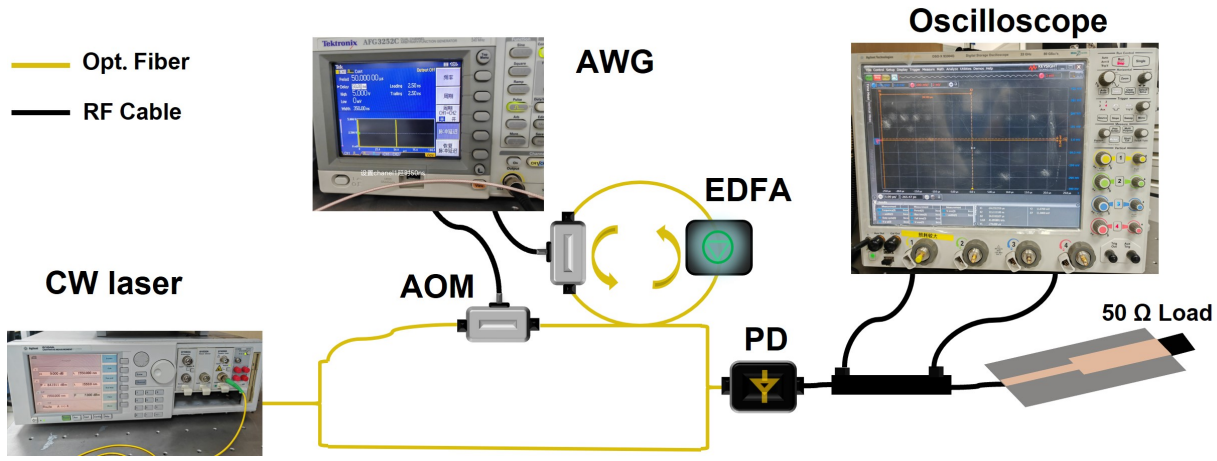

Fig. 9. Experiment setup

line with a relative dielectric constant of 9.6, the measurement range can be determined using Equation (11), which yields a maximum range of 24 mm. Therefore, to prevent time domain response from overlapping, the length of the DUT should not exceed 24 mm. For MUR simulation, two DUTs (DUT-1, DUT-5) were configured to exhibit a decreasing impedance pattern, featuring a narrow line initially, followed by a wider line, which introduces three discontinuities. As previously noted, DUT-1 was utilized as a reference unit for comparison. For DUT-5, the microstrip lines also had widths of 2 mm and 10 mm, but with corresponding lengths of 30 mm and 5 mm, respectively. Consequently, the spatial separation between connection A and B increased to 30 mm, facilitating the assessment of the system's MUR. Fig. 8(a) illustrates the results of DUT-1 simulation, with two peaks appear at the location of 10 mm and 15 mm, as expected. However, when the length of microstrip line increased to 30 mm, it will introduce time aliasing, as the total length of the DUT exceed the MUR of the system. As a consequence, the responses of connection B and C appear at positions other than their actual occurrence as shown in Fig. 8 (b). The alias-free range can be increased by adjusting the frequency step size Δf to a smaller value, in this case, 0.5 GHz. This modification results in the increase of MUR to 48 mm, thereby enabling to distinguish the two mismatches connection B and C apart, as depicted in Fig. 8(c).

V. EXPERIMENTAL RESULTS

A. *Experiment Setup*

The experiment implementation of the proposed system is shown in Fig. 9, which contains a wideband SF signal generation unit and a frequency response measurement unit. A continuous wave light with a wavelength of 1550 nm (Lightwave measurement Agilent 8164A) is divided into two paths through an optical coupler (50:50). In the upper branch, an AOM is modulated by an arbitrary function generator (Tektronix AFG3252C) with periodic pulse signal (duration 50 us, pulse width 350 ns) to serve as optical switch. The continuous light wave is subsequently truncated into periodic pulse signal and optically coupled into the recirculating OFSL. The output of the OFSL is progressively shifted by the AOM within the loop with fixed frequency step (200 MHz), which corresponds to AOM's driving RF frequency. An erbium-doped fiber amplifier (EDFA) is employed to compensate for the coupling losses. An optical bandpass filter with a bandwidth of 200 GHz is used to control the spectral range of the output signal and suppress unwanted noise.

Notably, the OFSL duration of 438.6 ns exceeds the 350 ns pulse width of the RF-modulated signal of AOM, which mitigates the potential interference between adjacent sub-pulse. The total duration for each sub pulse is designed to be sufficiently long to ensure that the reflected signal from the DUT does not overlap with the subsequent frequency sub-pulse. Moreover, in order to eliminate the fluctuation of signal amplitude within the loop, two polarization controllers are used both in the upper and down branch to reduce amplitude variation and the noise after repeated circulation. These configurations can effectively improve SNR of signal and increase the bandwidth, thereby obtaining high spatial resolution. In the upper branch, the output of OFSL is coupled out from the other

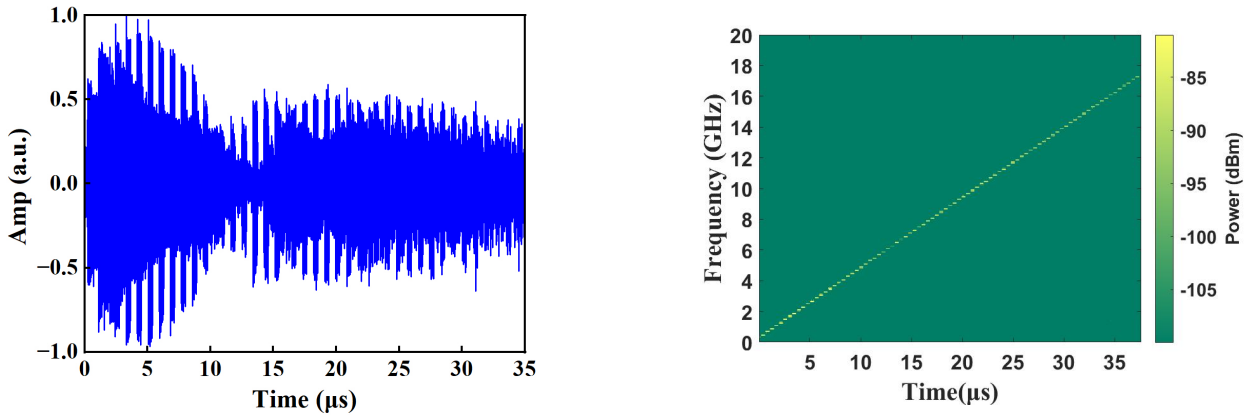

(a) (b)

Fig. 10. Measured wideband SF signal. (a) The temporal waveform and (b) the time and frequency spectrum.

OC and subsequently mixed with a portion of continuous wave light in the lower branch via a photodetector. This mixing progress generates an SF signal in the microwave domain.

The temporal waveforms of microwave SF signals generated by the MPSR system are presented in Fig. 10(a), with a total length of 35 μs. This timing arrangement is specifically designed to produce a sequence of 100 sub-pulses, enabling the generation of a wideband SF signal with a bandwidth of 20 GHz. Each period of the repetitive SF signals comprises 100 frequency-shifted sub-pulses, with a frequency increment of 200 MHz, yielding a cumulative bandwidth of 20 GHz. Fig. 10(b) represents the time-frequency relationship generated through short-term Fourier transform (STFT), demonstrating a steady and progressive increase in the carrier frequency of the SF signal. It is worth noting that the bandwidth of the SF signal is approximately 17 GHz, primarily due to the accumulated amplified spontaneous emission (ASE) noise in the OFSL, which contributes to amplitude fluctuations. As a result, for the subsequent defect detection experiment, the bandwidth of the SF signal is set to 16 GHz. This wideband SF signal is then injected through a direction coupler into the DUT. During the travelling along the DUT, the SF signal will be partially reflected when occurring impedance discontinuities. By mixing the reflected signal with input signal, frequency response of the DUT can be obtained. Subsequently, by applying IFFT to the frequency response, the time domain response can be reconstructed to define the location of discontinuity points. It is noteworthy that the frequency response of the DUT can be extracted by mixing the reflected signal with the reference signal via phase modulator and photodetector, and then passing the result through an optical bandpass filter to eliminate the negative first-order frequency component [36]. This process generates first-order sidebands in the frequency range from $f_c+\Delta f$ to $f_c+N\Delta f$, which falls in the same spectral range as the optical SF signal. Consequently, the mixing of these two signals results in a frequency-dependent phase difference, which corresponds to the frequency response of the DUT. The optical mixing process in the phase modulator and photodetector produces a demodulated signal that has low frequency, which can be easily captured and collected, reducing the reliance on high-end electronics. Nevertheless, to perform real-time spectrum analysis and assess the quality of the generated signal, a high-speed oscilloscope was utilized for sampling the signals and performing data mixing operations during the experiment.

B. Defect Detection Experiments

In the detection experiment, 4 PCB circuits were fabricated and used as DUTs, as shown in Fig. 11, each representing a unique testing scenario: impedance decrease (DUT-ID), impedance increase (DUT-II), range resolution (DUT-RR), and maximum unambiguous range (DUT-MUR). The substrate of PCB is F4B (PTFE-based), characterized with dielectric constant of 2.2, dielectric loss tangent of 0.001 and the thickness of 0.43 mm. By varying the width of microstrip line, impedance variation is effectively introduced within the DUT, enabling measurement of device's changing in electrical properties.

To quantify the time delay introduced by the RF cable and directional coupler at the points of signal injection and reflection, a preliminary experiment was performed without the DUT. The direction coupler was set in open-state condition to characterize the system's baseline response. The measurement results are shown in Fig. 12. Both the

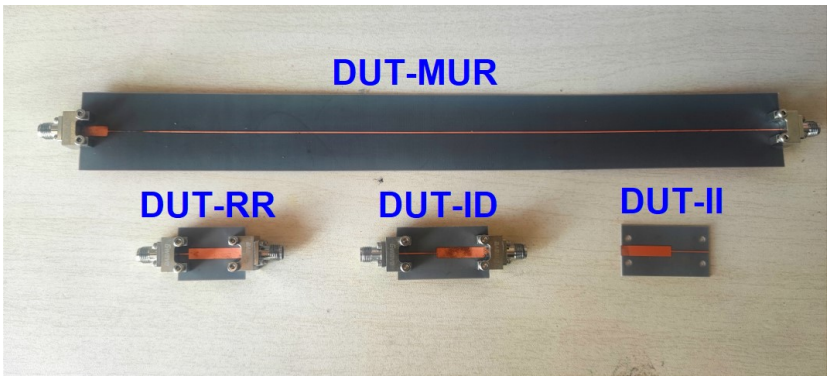

Fig. 11. Fabricated DUTs. DUT-ID, impedance decrease; DUT-II, impedance increase; DUT-RR, range resolution and DUT-MUR, maximum unambiguous range.

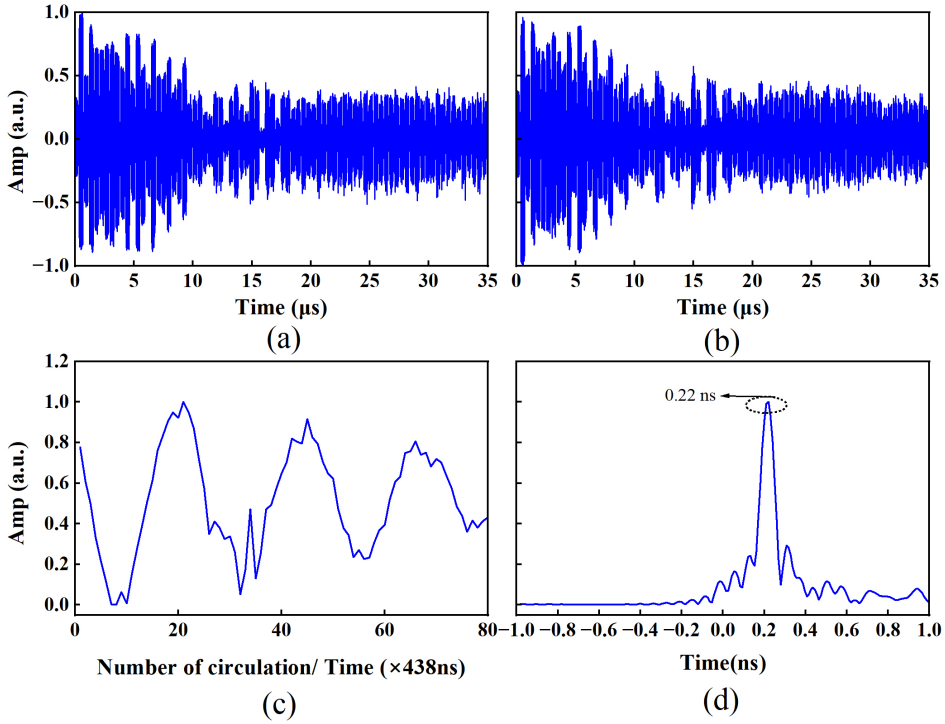

Fig. 12. Reference measurement. (a) Input signal temporal waveform, (b) output signal temporal waveform, (c) frequency response and (d) IFFT results.

incident and reflected signals were recorded in the oscilloscope. The oscilloscope's sampling rate is 80 GHz, which meets the Nyquist criterion that sampling rate of at least twice of the maximum frequency of interest, in this case, 16 GHz. This ensures that the oscilloscope can accurately capture the signal without time-aliasing. The incident signal, shown in Fig. 12(a) was mixed with the reflected signal as presented in Fig. 12(b), producing the frequency-domain response illustrated in Fig. 12(c). Taking the IFFT transform of the frequency response generates the time domain representation as displayed in Fig. 12(d). The directional coupler exhibits one distinct discontinuity, the open end, which is corroborated with the IFFT results of one prominent peak. In addition, the temporal separation between the peak and reference point corresponds to the time delay introduced by the directional coupler and RF cable, which is in good consistent with the time delay tested by VNA, that is 0.2 ns.

In the subsequent experiment, a proof-of-concept investigation was conducted, wherein two scenarios were considered: (1) impedance decrease scenario (DUT-ID), where the DUT consist of a narrow line in the first section and a wider line in the second section; (2) impedance increase scenario (DUT-II), which is achieved by simply

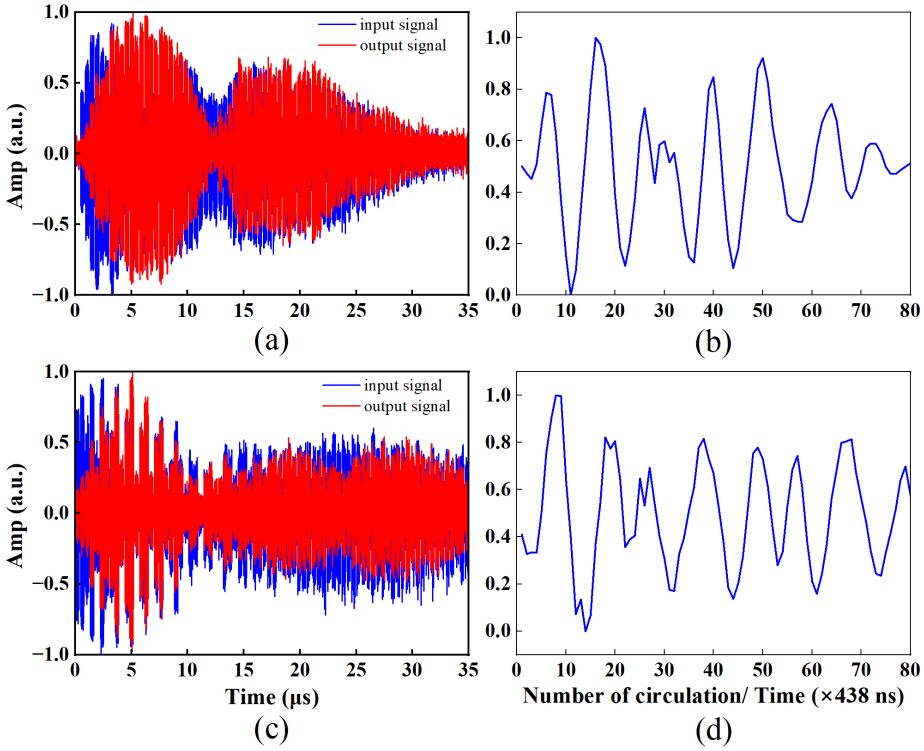

Fig. 13. Defect detection experiment results. (a) Input and output signal and (b) frequency response of impedance decrease experiment; (c) input and output signal and (d) frequency response of impedance increase experiment.

shift the orientation of the DUT. The DUT was set up with detachable SMA connectors on both ports, facilitating the connection with the directional coupler at the signal injection point and a 50-Ω load at the terminal point. This configuration is designed to minimize the impedance mismatch between the transmission line and the load, fascinating the implementation of the proposed reflectometry technique. For DUT-ID experiment, the width of microstrip lines was 0.5 mm and 4 mm with the corresponding length of 15 mm and 20 mm, respectively. The DUT-II experiment was conducted by simply reorienting the DUT-ID. The temporal waveforms of the incident and reflected signals obtained from these two experiments are presented in Fig. 13(a) and (c). By mixing the incident and reflected signals, the frequency responses of the two DUTs (DUT-ID, DUT-II) are generated, as illustrated in Fig. 13(b) and (d). Subsequent application of IFFT to the measured frequency response yields the resulting time-domain response of these two experiments, which are presented in Fig. 14(a) and (d). It is worth mentioning that, these IFFT results are plotted against time rather than range, due to the fact that the connectors on both ends may pose the bias in the range measurement. In a practical implementation, an initial measurement of the connector's length would be conducted, which would be subsequently subtracted from the original position to recalibrate the reference point. Taking into account of the time delay introduced by directional coupler and RF cable, the reconstructed IFFT results of MPSR are shown in Fig. 14(b) and (e). For clarity, we have labeled the key points as follows: A (injection point), B (second discontinuity), and C (third discontinuity). For DUT-ID, the separation between A and B was 15 mm, and between B and C was 20 mm. By reorienting the DUT-ID to form DUT-II, these distances were swapped, resulting in distances of 20 mm and 15 mm. The sequence of reflections began with the SF signal's entry into the DUT, generating the first reflection. Subsequent reflections were produced by the impedance discontinuities at points B and C, resulting in the second and third reflections, respectively, which are clearly visible as peaks B and C in Fig. 14 (b) and (e). In particular, the multiple reflections at the load at the end of the DUT contribute to the formation of an additional prominent peak. Notably, a microstrip line with the same configuration of DUT-ID, was simulated in ADS, yielding delays (including connector) of 0.12 ns and 0.22 ns for 15 mm and 35 mm length respectively, as shown in Fig.15. The time delays measured using the MPSR system were 0.13 ns and 0.25 ns, as illustrated in Fig. 14(b), with a deviation of approximately 0.03 ns from ADS simulation, which confirms the

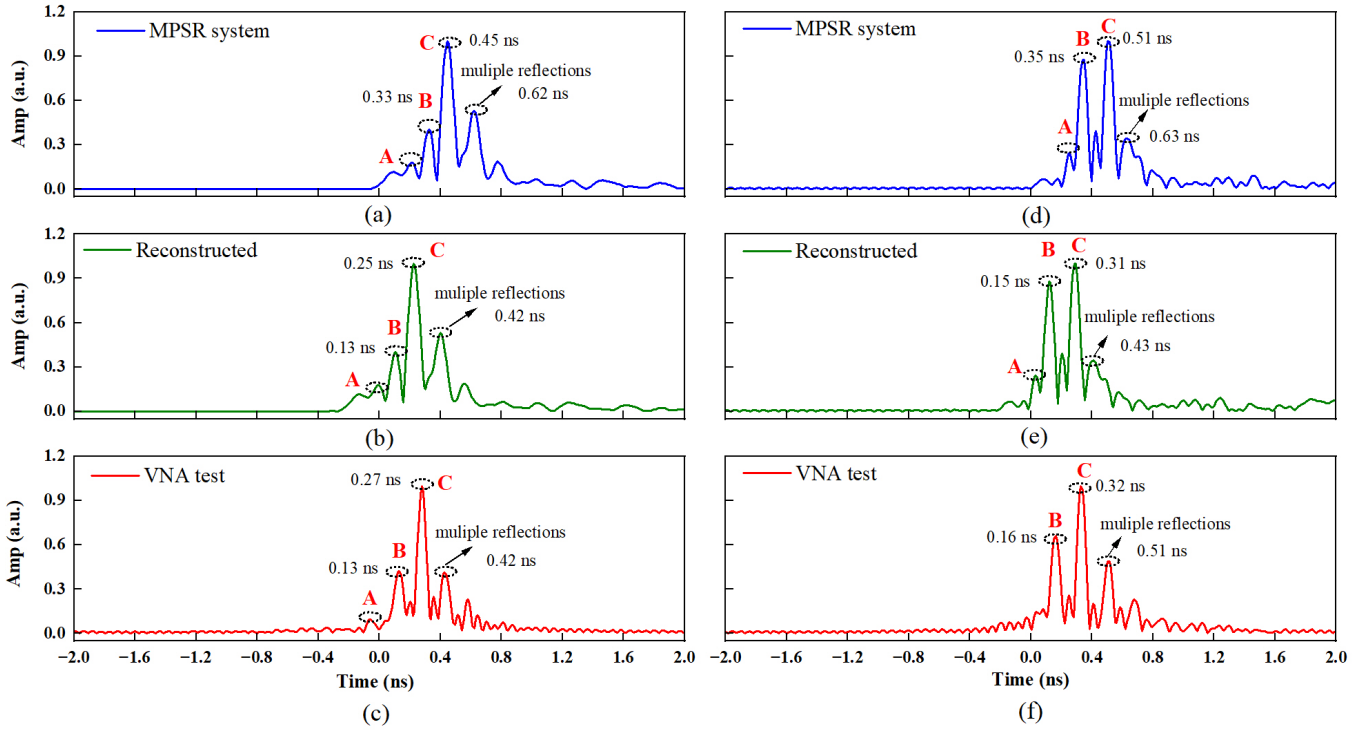

Fig. 14. IFFT results of impedance decrease and impedance increase experiments. The results of impedance decrease experiment based on (a) MPSR system, (b) reconstructed results of MPSR system and (c) VNA test ; (d)-(f) experimental results corresponding to the increase in impedance.

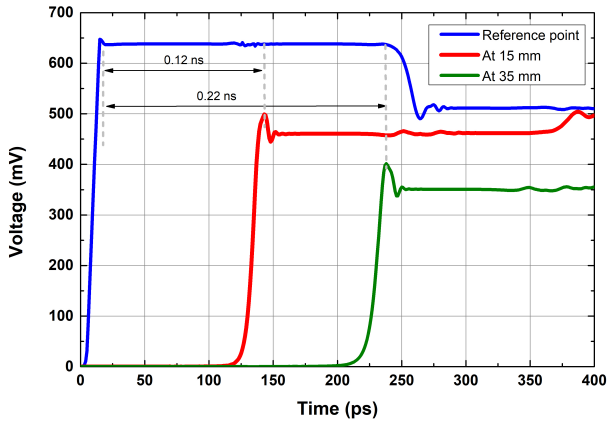

Fig. 15. The transient simulation for DUD-ID device.

accuracy and reliability of the proposed system. In addition, the S-parameter of DUT under VNA test was used as standard to compare with the MPSR measurements. This frequency-domain S-parameter was transformed into time domain via the IFFT, thus yielding the time-domain response of the DUT. The IFFT conversions of S parameter measured by VNA are presented in Fig. 14 (c) and (f). The IFFT results of MPSR are well agree with VNA test, with a small deviation of no more than 0.02 ns, validating the effectiveness and accuracy of the MPSR system in detecting impedance discontinuities.

C. The Range Resolution and Unambiguous Range Analysis of MPSR

To further investigate the detection features of the MPSR system, another three experiments were conducted: DUT-ID (with SF signal bandwidth of 6 GHz), range resolution (DUT-RR) and MUR (DUT-MUR), as displayed

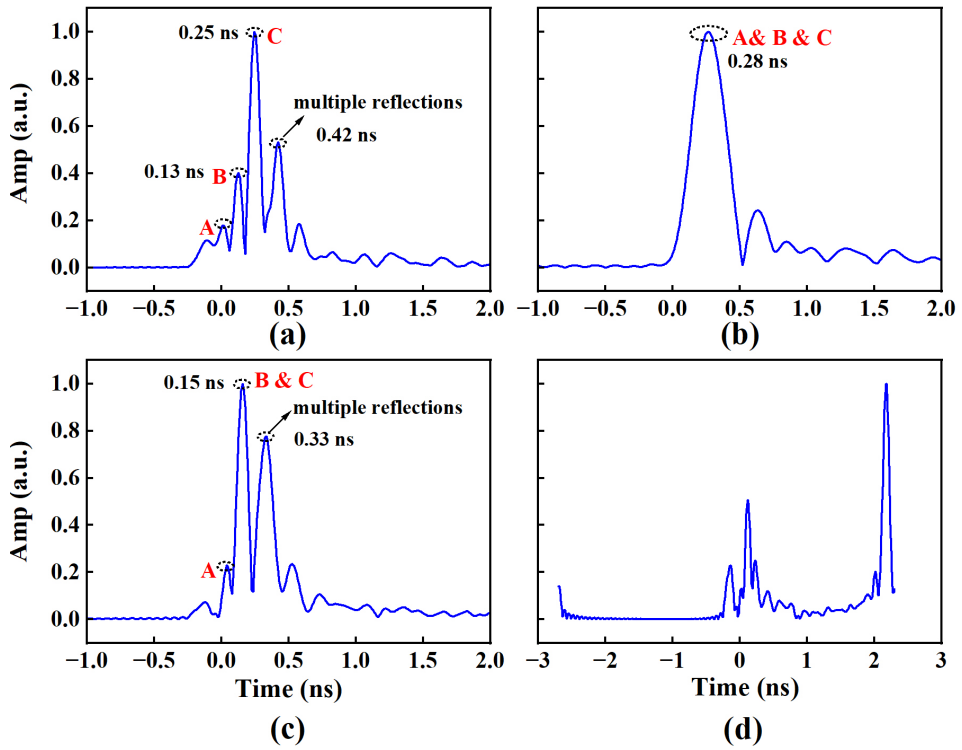

Fig. 16. Range resolution and MUR experiment results of MPSR system. IFFT results based on (a) DUT-ID, (b) DUT-ID (with SF signal bandwidth of 6 GHz), (c) DUT-RR and (d) DUT-MUR.

in Fig. 11. The range resolution experiment (DUT-RR) used microstrip lines with widths of 0.5 mm and 4 mm, and lengths of 4 mm and 21 mm. The MUR experiment (DUT-MUR) used microstrip lines with widths of 0.5 mm and 4 mm, and lengths of 260 mm and 10 mm. The performance of the three experiments was compared using DUT-ID (with SF signal bandwidth of 16 GHz) as a standard reference unit. We initially investigated the inverse relationship between wideband signal and range resolution, wherein a wideband signal is conducive to a higher range resolution. The time domain response of DUT-ID in Fig. 16(a) demonstrates that the utilization of the 16 GHz bandwidth signal exhibits a high degree of range resolution, allowing for the clear identification of three discontinuities as three distinct peaks, denoted as A, B, C in time domain. Conversely, the 6 GHz bandwidth case, suffering from a decreased range resolution, fail to resolve the discontinuities, which appear as a merged peak, denoted as peak A& B& C, as presented in Fig. 16(b). This degradation in performance is a direct consequence of the limited signal bandwidth. Furthermore, upon reducing the inter-discontinuity distance between connection B and C to 4 mm (DUT-RR), as depicted in Fig. 16(c), the corresponding discontinuities become indistinguishable (peak B&C) in the time-domain response. This observation highlights the system's limited range resolution, leading to insufficiency in resolving discontinuities. The theoretical range resolution as given by $\Delta R = \frac{v}{2B}$, yields a value of approximately 6.3 mm for an 16 GHz bandwidth signal. This range resolution of 6.3 mm imposes a fundamental constraint on the system's ability to resolve closely spaced discontinuities. Consequently, features separated by distance below this threshold are irresolvable from IFFT results, and instead appear as a single, merged peak, rather than distinct peaks corresponding to individual discontinuities.

In the MUR experiment, as previous noted, the process of sampling in frequency domain inherently introduces the risk of time aliasing. Specifically, when frequency domain data is discrete sampled, the time domain content will be folded back into the unambiguous range, thereby generated aliasing artifact that can reduce the accuracy of measured data. As predicted by the formula for $MUR = \frac{v}{2\Delta f}$, the calculated MUR is approximately 253 mm with frequency step of 200 MHz, defining the range interval within which discontinuities can be uniquely identified without aliasing artifacts. Fig. 16(d) illustrates that when the distance between two discontinuities (260 mm) surpasses the MUR (253 mm), time aliasing occurs, resulting in a distorted time-domain response. As a consequence, the time domain response was folded back into the unambiguous range, causing them to appear at

TABLE I. Comparison with other defect detection techniques

Technique	Resolution	Working bandwidth	Single measurement time	Electrical characteristic detection	Limitation
X-ray [1], [2]	Sub-centimeter level	-	-	No	High-power damage
AOI [7], [8]	Sub-centimeter level	-	-	No	Substantial training data and significant computational resources
TDR [14]	Meter level	96 MHz	-	Yes	Fast rise-time signal
FDR [15]	Meter level	400 MHz	-	Yes	Operating bandwidth limited by electronics
SFWR [17]	Meter level	50 MHz	0.2 ms	Yes	Operating bandwidth limited by electronics
Our work	Sub-centimeter level	16 GHz	35 μs	Yes	-

the times that are inconsistent with their temporal locations, leading to ambiguity and error into the measurement.

The comparison with other defect detection techniques is listed in Tab.I. Based on the x-ray and camera images, the X-ray and AOI methods can provide resolution of sub-centimeter level, however, it can not ensure the electrical characteristic detection performance. The traditional TDR, FDR and SFWR, with bandwidth less than 1 GHz and meter level resolution, are usually used for defect detection of long cables, which are not suitable for integrated electronic circuit diagnosis. Utilizing microwave photonic techniques, the proposed MPSR system with a bandwidth of 16 GHz achieved a substantial enhancement in the range resolution (sub-centimeter level). To sum up, the proposed MPSR system features a wide bandwidth and high resolution, which can be further implemented in highly integrated electronic module defect detection.

VI. CONCLUSION

A novel microwave photonic step frequency reflectometry (MPSR) system with a sub centimeter resolution has been proposed and demonstrated. By combining the strengths of photonic technology in wideband signal generation, and the advantages of reflectometry in electrical characteristic identification, this approach delivers a robust and accurate method for detecting defects in electronic circuit. Facilitated by the optical frequency shift loop (OFSL) technique, a wideband incident signal can be generated using a relatively narrowband electronic signal generator, eliminating the demand for high-end electronics. In the experiment, broadband step frequency signal with 16-GHz bandwidth was generated to serve as incident signal in MPSR system, achieving a sub centimeter resolution, which is approximately 6.3 mm. The experimental findings of clear identification and location of three impedance discontinuities within the DUT confirm the system's capability in spatially resolving information about the internal structure of the DUT, thereby enabling accurate characterization and analysis of its defects. Moreover, the proposed system's performance metrics, including range resolution and unambiguous range can be substantially improved by increasing the signal bandwidth and decreasing the frequency step. Further research can be taken to extend this approach in advanced packing defect detection, such as through-silicon via (TSV), system-in-package (SiP), and 3D stacked integration, to meet the increasing demand for miniaturization of electronics.

REFERENCES

[1] A. Du Plessis, I. Yadroitsev, I. Yadroitsava, and S. G. Le Roux, "X-ray microcomputed tomography in additive manufacturing: a review of the current technology and applications," *3D Print. Addit. Manuf.*, vol. 5, no. 3, pp. 227–247, 2018.

[2] B. C. Wolz, C. Jaremenko, F. Vollnhals, L. Kling, J. Wrege, and S. Christiansen, "X-ray microscopy and automatic detection of defects in through silicon vias in three-dimensional integrated circuits," *Eng. Rep.*, vol. 4, no. 12, p. e12520, 2022.

[3] H. Weng, D. G. Beetner, and R. E. DuBroff, "Prediction of radiated emissions using near-field measurements," *IEEE Trans. Electromagn. Compat.*, vol. 53, no. 4, pp. 891–899, 2011.

[4] Z. He, L. Wang, and Q. H. Liu, "Enhanced defect detection in rf circuits using dm-srm and elastic regularization techniques," vol. 72, no. 9, pp. 5134–5142, 2024.

[5] F. Feng, W. Na, J. Jin, J. Zhang, W. Zhang, and Q.-J. Zhang, "Artificial neural networks for microwave computer-aided design: The state of the art," *IEEE Trans. Microw. Theory Tech.*, vol. 70, no. 11, pp. 4597–4619, 2022.

[6] J. Jin, C. Zhang, F. Feng, W. Na, J. Ma, and Q.-J. Zhang, "Deep neural network technique for high-dimensional microwave modeling and applications to parameter extraction of microwave filters," *IEEE Trans. Microw. Theory Tech.*, vol. 67, no. 10, pp. 4140–4155, 2019.

[7] H. Y. Ma, M. Xia, Z. Gao, and W. Ye, "Automated void detection in high resolution x-ray printed circuit boards (pcbs) images with deep segmentation neural network," *Eng. Appl. Artif. Intell.*, vol. 133, p. 108425, 2024.

[8] Q. Ling and N. A. M. Isa, "Printed circuit board defect detection methods based on image processing, machine learning and deep learning: A survey," *IEEE Access*, vol. 11, pp. 15 921–15 944, 2023.

[9] P. Chen and F. Xie, "A machine learning approach for automated detection of critical pcb flaws in optical sensing systems," in *Photonics*, vol. 10, no. 9. MDPI, 2023, p. 984.

[10] J.-H. Park, Y.-S. Kim, H. Seo, and Y.-J. Cho, "Analysis of training deep learning models for pcb defect detection," *Sensors*, vol. 23, no. 5, p. 2766, 2023.

[11] M. K. Smail, L. Pichon, M. Olivas, F. Auzanneau, and M. Lambert, "Detection of defects in wiring networks using time domain reflectometry," *IEEE Trans. Magn.*, vol. 46, no. 8, pp. 2998–3001, 2010.

[12] C. M. Furse, M. Kafal, R. Razzaghi, and Y.-J. Shin, "Fault diagnosis for electrical systems and power networks: A review," *IEEE Sensors J.*, vol. 21, no. 2, pp. 888–906, 2020.

[13] S. Kingston, E. Benoit, A. S. Edun, F. Elyasichamazkoti, D. E. Sweeney, J. B. Harley, P. K. Kuhn, and C. M. Furse, "A sstdr methodology, implementations, and challenges," *Sensors*, vol. 21, no. 16, p. 5268, 2021.

[14] E. Benoit, S. J. Hansen, S. R. Kingston, J. B. Harley, and C. M. Furse, "Capability of impedance measurement using spread spectrum time-domain reflectometry," *IEEE Trans. Instrum. Meas.*, vol. 72, pp. 1–9, 2023.

[15] C. Furse, Y. C. Chung, R. Dangol, M. Nielsen, G. Mabey, and R. Woodward, "Frequency-domain reflectometry for on-board testing of aging aircraft wiring," *IEEE Trans. Electromagn. Compat.*, vol. 45, no. 2, pp. 306–315, 2003.

[16] K. Yuksel, M. Wuilpart, V. Moeyaert, and P. Mégret, "Optical frequency domain reflectometry: A review," in *2009 11th International Conference on Transparent Optical Networks*. IEEE, 2009, pp. 1–5.

[17] C.-K. Lee, G.-Y. Kwon, and Y.-J. Shin, "Condition assessment of i&c cables in nuclear power plants via stepped-frequency waveform reflectometry," *IEEE Trans. Instrum. Meas.*, vol. 68, no. 1, pp. 215–224, 2019.

[18] Y. H. Lee, G.-Y. Kwon, and Y.-J. Shin, "Contactless monitoring technique for live shielded cable via stepped-frequency waveform reflectometry and inductive coupler," *IEEE Trans. Ind. Electron.*, vol. 69, no. 9, pp. 9494–9503, 2022.

[19] J.-M. Wun, C.-C. Wei, J. Chen, C. S. Goh, S. Set, and J.-W. Shi, "Photonic chirped radio-frequency generator with ultra-fast sweeping rate and ultra-wide sweeping range," *Opt. Express*, vol. 21, no. 9, pp. 11 475–11 481, 2013.

[20] A. Kanno and T. Kawanishi, "Broadband frequency-modulated continuous-wave signal generation by optical modulation technique," *J. Lightw. Technol.*, vol. 32, no. 20, pp. 3566–3572, 2014.

[21] A. Yacoubian and P. K. Das, "Digital-to-analog conversion using electrooptic modulators," *IEEE Photon. Technol. Lett.*, vol. 15, no. 1, pp. 117–119, 2003.

[22] T. Hao, Q. Cen, Y. Dai, J. Tang, W. Li, J. Yao, N. Zhu, and M. Li, "Breaking the limitation of mode building time in an optoelectronic oscillator," *Nat. Commun.*, vol. 9, no. 1, p. 1839, 2018.

[23] Z. Tang, Y. Li, J. Yao, and S. Pan, "Photonics-based microwave frequency mixing: methodology and applications," *Laser & Photonics Rev.*, vol. 14, no. 1, p. 1800350, 2020.

[24] E. A. Kittlaus, D. Eliyahu, S. Ganji, S. Williams, A. B. Matsko, K. B. Cooper, and S. Forouhar, "A low-noise photonic heterodyne synthesizer and its application to millimeter-wave radar," *Nat. Commun.*, vol. 12, no. 1, p. 4397, 2021.

[25] B. Li, W. Wei, D. Han, W. Xie, and Y. Dong, "Remote broadband rf signal down-conversion with stable phase and high efficiency using a sideband optical phase-locked loop," *Opt. Express*, vol. 28, no. 9, pp. 12 588–12 598, 2020.

[26] S. Pan and Y. Zhang, "Microwave photonic radars," *J. Lightw. Technol.*, vol. 38, no. 19, pp. 5450–5484, 2020.

[27] P. Ghelfi, F. Laghezza, F. Scotti, G. Serafino, A. Capria, S. Pinna, D. Onori, C. Porzi, M. Scaffardi, A. Malacarne *et al.*, "A fully photonics-based coherent radar system," *Nature*, vol. 507, no. 7492, pp. 341–345, 2014.

[28] L. Yi, R. Kaname, R. Mizuno, Y. Li, M. Fujita, H. Ito, and T. Nagatsuma, "Ultra-wideband frequency modulated continuous wave photonic radar system for three-dimensional terahertz synthetic aperture radar imaging," *J. Lightw. Technol.*, vol. 40, no. 20, pp. 6719–6728, 2022.

[29] D. Zhu, W. Chen, J. Ding, C. Ma, Y. Yang, X. Hu, and S. Pan, "Microwave photonic cognitive radar with a subcentimeter resolution," *IEEE Trans. Microw. Theory Tech.*, 2024.

[30] T. Shi, Y. Chen, and J. Yao, "Seamlessly merging radar ranging and imaging, wireless communications, and spectrum sensing for 6g empowered by microwave photonics," *Comms. Eng.*, vol. 3, no. 1, p. 130, 2024.

[31] G. Sun, F. Zhang, K. Zhao, and S. Pan, "Photonics-based broadband vortex electromagnetic wave generation for high-resolution imaging," *J. Lightw. Technol.*, vol. 42, no. 6, pp. 1894–1900, 2024.

[32] Z. Zhang, Y. Liu, T. Stephens, and B. J. Eggleton, "Photonic radar for contactless vital sign detection," *Nat. Photonics*, vol. 17, no. 9, pp. 791–797, 2023.

[33] C. Schnébelin, J. Azaña, and H. Guillet de Chatellus, "Programmable broadband optical field spectral shaping with megahertz resolution using a simple frequency shifting loop," *Nat. Commun.*, vol. 10, no. 1, p. 4654, 2019.

[34] Y. Lyu, Y. Li, C. Yu, L. Yi, T. Nagatsuma, and Z. Zheng, "Photonic generation of highly-linear ultra-wideband stepped-frequency microwave signals with up to 6· 10 6 time-bandwidth product," *J. Lightw. Technol.*, vol. 40, no. 4, pp. 1036–1042, 2021.

[35] Y. Zhang, C. Liu, Y. Zhang, K. Shao, C. Ma, L. Li, L. Sun, S. Li, and S. Pan, "Multi-functional radar waveform generation based on optical frequency-time stitching method," *J. Lightw. Technol.*, vol. 39, no. 2, pp. 458–464, 2020.

[36] Y. Liu, Z. Zhang, M. Burla, and B. J. Eggleton, "11-ghz-bandwidth photonic radar using mhz electronics," *Laser & Photonics Rev.*, vol. 16, no. 4, p. 2100549, 2022.

[37] Z. Zhang, Y. Liu, and B. J. Eggleton, "Photonic generation of 30 ghz bandwidth stepped-frequency signals for radar applications," *J. Lightw. Technol.*, vol. 40, no. 14, pp. 4521–4527, 2022.

[38] C. Nguyen, J. Park, C. Nguyen, and J. Park, *Stepped-Frequency Radar Sensors: Theory, Analysis and Design*. Springer, 2016.

Yiling Guo received the B.S. degree from Huaqiao University, Quanzhou, China, and the M.S. degree in Queen Mary University of London, in 2012 and 2017, respectively. She is currently a research student with the Department of Electrical and Electronic Engineering at Hong Kong Polytechnic University under the supervision of Dr. Menglin Chen. Her current research interests include microwave photonics, electronic circuit defect detection and RF circuit design.

Mingtuan Lin received the B.Sc., M.Sc. and PhD. degrees in electronic science and technology from the National University of Defense Technology, Changsha, China, in 2012, 2014 and 2018, respectively, under the supervision of Prof. P.G. Liu. He had been a Visiting Ph.D. Student with the Queen Mary University of London, London, U.K., since 2015, under the guidance of Dr. Y. Gao. He is currently an Associate Professor in National University of Defense Technology. His current research interests include microwave photonics, dynamic-metamaterial-based antenna and array signal processing.

Wei Lin (Senior Member, IEEE) received the Ph.D. degree in Electronic Engineering from the City University of Hong Kong, Hong Kong SAR China, in 2016. He received the bachelor's and master's degrees from the South China University of Technology, Guangzhou, China, in 2009 and 2012, respectively. Dr Lin is currently an Assistant Professor with the Department of Electrical and Electronic Engineering, The Hong Kong Polytechnic University, Hong Kong SAR, China. He is also a member of State Key Laboratory of Terahertz and Millimeter Waves at the City University of Hong Kong. Dr Lin was a Visiting Lecturer with the University College London, London, the United Kingdom from July to Sep. 2022. He was a Post-Doctoral Research Associate from October 2016 to September 2018, and then a Chancellor's Post-Doctoral Research Fellow, from October 2018 to May 2021, and then a Lecturer and ARC DECRA Fellow from May 2021 to Sep. 2022 with the Global Big Data Technologies Centre, the University of Technology Sydney (UTS), Ultimo, NSW, Australia. He worked as a Research Associate with Nanyang Technological University, Singapore, from August 2012 to August 2013. His research interests include antennas and radioactive circuits, applied electromagnetics, wireless power transfer for IoT system, microwave, millimetre-wave and terahertz devices, and their applications. Dr Lin has received many academic awards, which mainly include the Australia Research Council (ARC) Discovery Early Career Researcher Award (DECRA2021), the 2019 Raj Mittra Travel Grant (RMTG2019) from the IEEE AP-Society, the Best Paper Award (First Prize) at the International Symposium on Antennas and Propagation (ISAP 2018), the Best Young Professional Paper Award (First prize) at the 3rd Australian Microwave Symposium (AMS2018), the Best Poster Paper Award at the 2nd International Conference on Electromagnetic Materials and Technologies for the Future (EM-MTF2017), a Talent Development Scholarship from the Hong Kong Government, and the Young Scientist Award at the IEEE Region 10 Conference (TENCON2015). Dr Lin was the 2022 IEEE AP-S Young Professional Ambassador and is the Associate Editor of IEEE Transactions on Antennas and Propagation.

Shilie Zheng (Member, IEEE) received the B.S. and M.S. degrees in materials science and the Ph.D. degree in physical electronics from Zhejiang University, Hangzhou, China, in 1995, 1998, and 2003, respectively. In 1998, she joined the Department of Information Science and Electronic Engineering, Zhejiang University, where she was appointed as an Associate Professor in 2005. From November 2005 to March 2006, she spent five months with Tohoku University, Sendai, Japan, as a Research Assistant. From July 2016 to July 2017, she was a Visiting Research Fellow with the RF and microwave Laboratory, National University of Singapore, Singapore. In 2017, she was appointed as a Full Professor with Zhejiang University. Her current research interests include microwave photonics, twisted radio waves and applications, and wireless communications.

Menglin Chen (Senior Member, IEEE) received the B.S. degree from Huazhong University of Science and Technology, Wuhan, China, the B.Eng. degree from the University of Birmingham, U.K., in 2012, the M.S. degree and the Ph.D. degree from the University of Hong Kong, Hong Kong, in 2013 and 2018, respectively. From May 2017 to October 2017, she had been an Academic Visitor with the School of Electronic Engineering and Computer Science at Queen Mary University of London. From 2018 to 2022, she was a Post-Doctoral Fellow at the University of Hong Kong. She is currently a Research Assistant Professor with the Department of Electrical and Electronic Engineering at Hong Kong Polytechnic University. Her research interests include advanced electromagnetics-based interdisciplinary research, including novel metamaterial/metasurface design, microwave photonics, topological photonic crystals, and their applications in microwave/millimeter wave engineering.